JOURNAL OF SOLID STATE CHEMISTRY

Volume 179, Number 5, May 2006

CONTENTS

Editorial Announcement
Mercouri G. Kanatzidis
Page 1295

Regular Articles

A novel ferrimagnetic irido-cuprate: $IrSr_2GdCu_2O_8$
A.J. Dos Santos-García, Myriam H. Aguirre, E. Morán, R. Saez Puche and M.Á. Alario-Franco
Page 1296

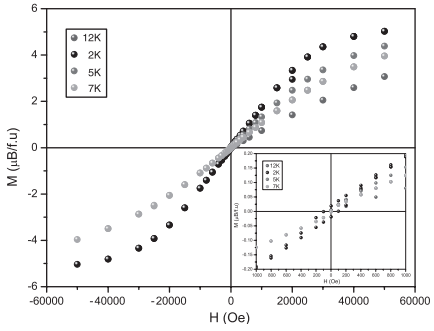

$IrSr_2GdCu_2O_8$, prepared under high-temperature and high-pressure conditions, is a new member of the M-1212-type cuprates. A ferrimagnetic Ir^{IV}–Gd^{III} spin ordering is observed below 15 K. The iridium oxidation state seems to be +4, while the copper oxidation state is $Cu^{+2.5}$.

Electron doping effect on structural and magnetic phase transitions in $Sr_{2-x}Nd_xFeMoO_6$ double perovskites
A.K. Azad, S.-G. Eriksson, Abdullah Khan, A. Eriksson and M. Tseggai
Page 1303

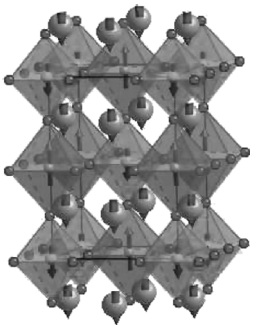

3D ferrimagnetic structure of $Sr_{2-x}Nd_xFeMoO_6$ below Curie temperature.

Regular Articles—Continued

$[Zn_2(HPO_3)_2(H_2PO_3)][C_3H_5N_2]$ and $[Zn_2(HPO_3)_3][C_4H_7N_2]_2 \cdot 2H_2O$: Two new layered zinc phosphites with double 12-membered rings templated by imidazole and 2-methylimidazole
Li Liu, Yunling Liu, Guanghua Li, Chao Chen, Minghui Bi and Wenqin Pang
Page 1312

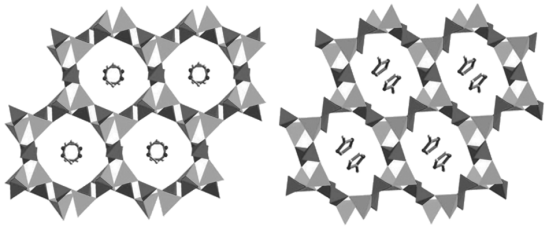

Polyhedral views of the double layer structures of $[Zn_2(HPO_3)_2(H_2PO_3)][C_3H_5N_2]$ and $[Zn_2(HPO_3)_3][C_4H_7N_2]_2 \cdot 2H_2O$ showing the imidazole cations sitting in the middle of the D12MR windows and 2-methylimidazole cations inserting into the D12MR cavities.

Synthesis, structure and properties of a new Zintl phase: SrLiSb
Shalabh Gupta and Ashok K. Ganguli
Page 1318

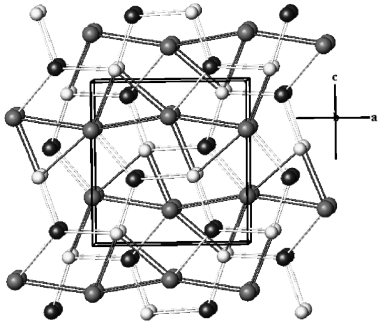

An ~[010] representation of the structure of SrLiSb. Indigo represent antimony atoms surrounded by red and the yellow spheres representing strontium and lithium atoms respectively forming the corners of trigonal prisms. The trigonal prisms are linked through Sr forming the zig-zag chains of trigonal prismatic columns.

New representatives of the linear structure series containing empty Ga/Ge cubes in the Sm–Ga–Ge system
Yaroslav O. Tokaychuk, Yaroslav E. Filinchuk, Anatoliy O. Fedorchuk, Artem Yu. Kozlov and Ivanna R. Mokra
Page 1323

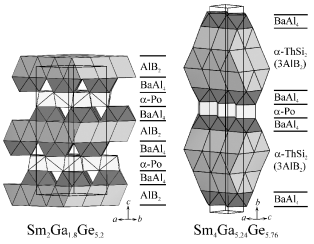

The structures of the new ternary compounds $Sm_2Ga_{7-x}Ge_x$ ($x = 5.2-6.1$) and $Sm_4Ga_{11-x}Ge_x$ ($x = 5.76-8.75$) belong to the linear intergrowth structure series built up from the segments of $BaAl_4$, AlB_2 and α-Po structure types. The Ga/Ge networks in these structures contain characteristic empty cubes with one side capped by Ga atoms, which display an intrinsic displacive atomic disorder.

The effects of $ZnGa_2O_4$ formation on structural and optical properties of ZnO:Ga powders
Agnaldo de Souza Gonçalves, Sergio Antonio Marques de Lima, Marian Rosaly Davolos, Selma Gutierrez Antônio and Carlos de Oliveira Paiva-Santos
Page 1330

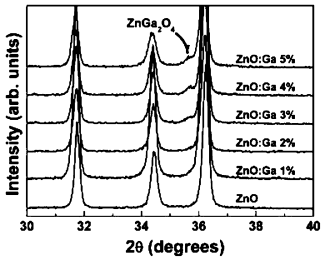

Zoomed powder X-ray diffraction patterns of pure and gallium-doped zinc oxide samples.

Solid triphenylmethanol: A molecular material that undergoes multiple internal reorientational processes on different timescales
Simon J. Kitchin, Mingcan Xu, Heliodoro Serrano-González, Laura J. Coates, S. Zaka Ahmed, Christopher Glidewell and Kenneth D.M. Harris
Page 1335

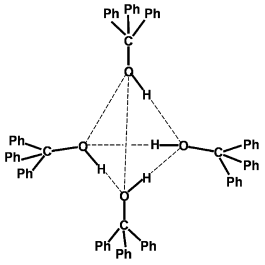

In solid triphenylmethanol, the molecules are arranged in hydrogen-bonded tetramers as shown; dynamic properties of this material are investigated here using solid-state ^2H NMR spectroscopy.

Compatibility evaluation between $La_2Mo_2O_9$ fast oxide-ion conductor and Ni-based materials
Gwenaël Corbel and Philippe Lacorre
Page 1339

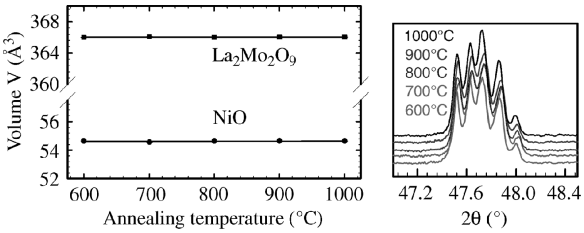

The absence of chemical reaction between Ni or NiO and $La_2Mo_2O_9$ up to 1000 °C, evidenced by room temperature X-ray powder diffraction, makes Ni-based cermet potential anode materials for LAMOX electrolyte.

Synthesis, structure, and characterization of a new one-dimensional tellurite phosphate, $Ba_2TeO(PO_4)_2$
Kang Min Ok and P. Shiv Halasyamani
Page 1345

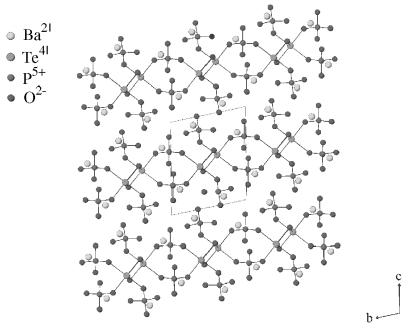

Ball-and-stick diagram showing one-dimensional structure of $Ba_2TeO(PO_4)_2$ in the *bc*-plane. Note the chains run along the *b*-axis.

Highly ordered MnO_2 nanowire array thin films on Ti/Si substrate as an electrode for electrochemical capacitor
Cai-Ling Xu, Shu-Juan Bao, Ling-Bin Kong, Hua Li and Hu-Lin Li
Page 1351

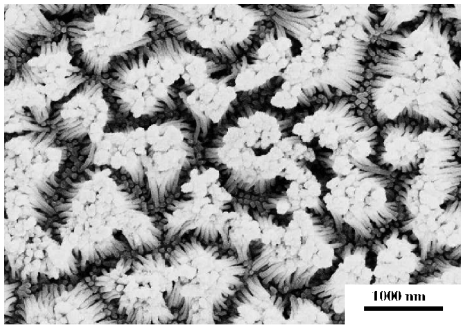

FESEM image of MnO_2 nanowire arrays grown on AAO/Ti/Si substance.

Continued

Luminescence of $NaGdFPO_4$:Ln^{3+} after VUV excitation: A comparison with $GdPO_4$:Ln^{3+} (Ln = Ce, Tb)
Zifeng Tian, Hongbin Liang, Huihong Lin, Qiang Su, Bei Guo, Guobin Zhang and Yibing Fu
Page 1356

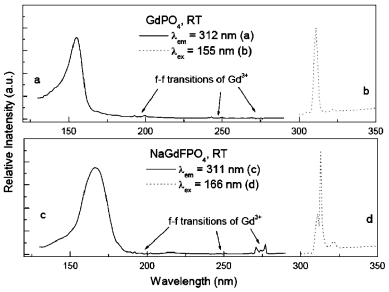

The VUV excitation (a, under emission at 312 nm) and VUV-excited emission (b, excitation under 155 nm) spectra for phosphor $GdPO_4$ at 293 K, the VUV excitation (c, under emission at 311 nm) and VUV-excited emission (d, excitation under 166 nm) spectra for phosphor $NaGdFPO_4$ at 293 K.

Single crystal structure and Raman spectrum of $Ba_3Na_2(CN_2)_4$
Yongkwan Dong and Francis J. DiSalvo
Page 1363

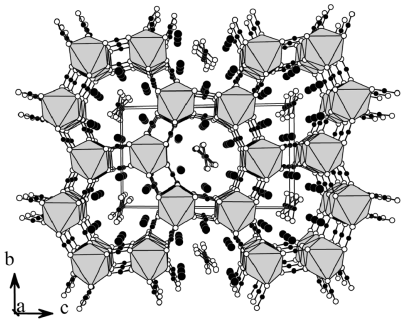

The crystal structure of $Ba_3Na_2(NCN)_4$ along the [100] direction.

Combined powder neutron and X-ray diffraction study of charge and orbital order in $Bi_{0.75}Sr_{0.25}MnO_3$
R.J. Goff and J.P. Attfield
Page 1369

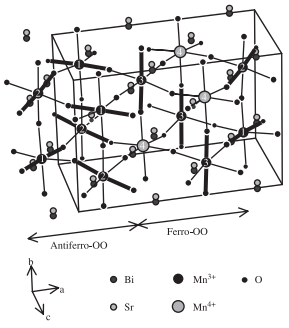

A model for charge and orbital order in $Bi_{0.75}Sr_{0.25}MnO_3$ is proposed from a high-resolution powder X-ray and neutron diffraction study. An ordered intergrowth of antiferro-orbitally ordered ($LaMnO_3$ type) and charge and ferro-orbitally ordered ($YBaMn_2O_6$ type) blocks is found, in agreement with previous electron microscopy images.

Charge and structural ordering in the brownmillerite phases: $La_{1-x}Sr_xMnO_{2.5}$ ($0.2 < x < 0.4$)
Peter S. Casey, Daniel Barker and Michael A. Hayward
Page 1375

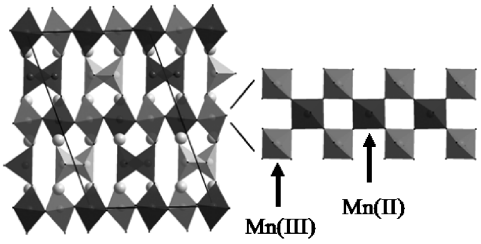

Charge ordering in the octahedral layers of $La_{0.75}Sr_{0.25}MnO_{2.5}$.

Amorphous and nanocrystalline titanium nitride and carbonitride materials obtained by solution phase ammonolysis of $Ti(NMe_2)_4$
Andrew W. Jackson, Olga Shebanova, Andrew L. Hector and Paul F. McMillan
Page 1383

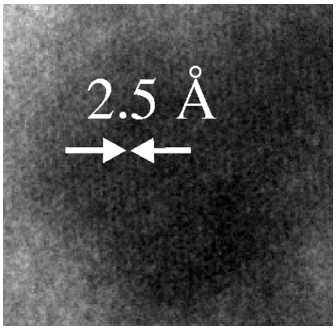

Amorphous and nanocrystalline titanium nitrides and carbonitrides with a very defect-rich rocksalt structure.

Transport, magnetic, internal friction, and Young's modulus in the Y-doped manganites $La_{0.9-x}Y_xTe_{0.1}MnO_3$
G.H. Zheng, Y.P. Sun, X.B. Zhu and W.H. Song
Page 1394

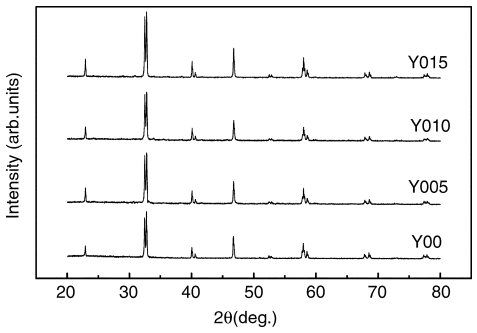

XRD patterns of the compound $La_{0.9-x}Y_xTe_{0.1}MnO_3$ ($x = 0$, 0.05, 0.10, 0.15).

Antiferromagnetic ordering with an anisotropy reversal in $USn_{0.5}Sb_{1.5}$

V.H. Tran, Z. Bukowski, J. Stępień-Damm and R. Troć

Page 1401

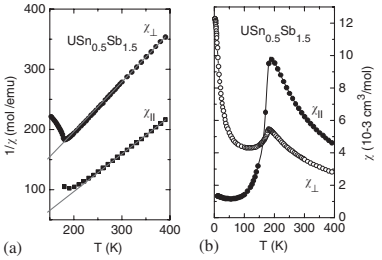

(a) Temperature dependence of the reciprocal magnetic susceptibility of $USn_{0.5}Sb_{1.5}$ measured perpendicular ($\chi_\perp$) and along ($\chi_\parallel$) to the *c*-axis. (b) Magnetic susceptibility as a function of temperature.

Layer-by-layer assembly of multilayer films of polyoxometalates and tris(phenanthrolinedione) complexes of transition metals

Shuiying Gao, Xing Li, Chunpeng Yang, Taohai Li and Rong Cao

Page 1407

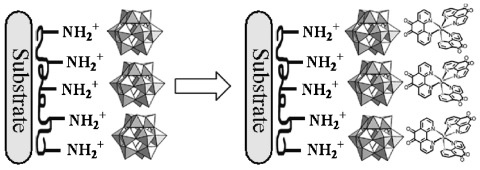

A series of organic–inorganic composite films ($BW_{12}/[M(phendione)_3]^{2+})_n$ ($M=Fe^{2+}$, Co^{2+}) and ($Co_4(PW_9)_2/[M(phendione)_3]^{2+})_n$ ($M=Fe^{2+}$, Co^{2+}, phendione = 1,10-phenanthroline-5,6-dione) were prepared by the layer-by-layer self-assembly method. The films exhibit well-defined electrochemical behaviors. Moreover, electrochemical behavior of the phendione species is pH dependent. The multilayer films have potential application in electrochemical sensors.

Synthesis, structure and optical limiting effect of a novel inorganic–organic hybrid polymer containing mixed chains of copper(I)/iodine

Hao-Hong Li, Zhi-Rong Chen, Jun-Qian Li, Hong-Bing Zhan, Wen-Xuan Zhang, Chang-Cang Huang, Cheng Ma and Bin Zhao

Page 1415

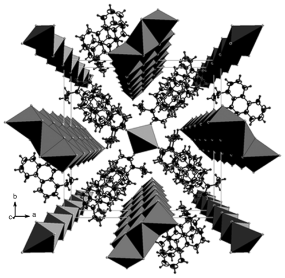

An unusual coordination polymer $[(ebq)_2(Cu_3I_4)(CuI_2)]_n$ (**1**) has been synthesized and characterized. A highly interesting feature of **1** is its presence of mixed types of chains $[(Cu_3I_4)_n^-$ and $(CuI_2)_n^-$ chain] in one crystal lattice based on supramolecular self-assembly directed by cations. The infinite chains $(Cu_3I_4)_n^-$ and $(CuI_2)_n^-$ in **1** could be described as the edge-sharing arrangement of CuI_4 tetrahedron. The optical limiting experiments show that the present polymer exhibits a large optical limiting capacity.

Template synthesis and characterization of $PbTiO_3$ nanowire arrays from aqueous solution

M.C. Hsu, I.C. Leu, Y.M. Sun and M.H. Hon

Page 1421

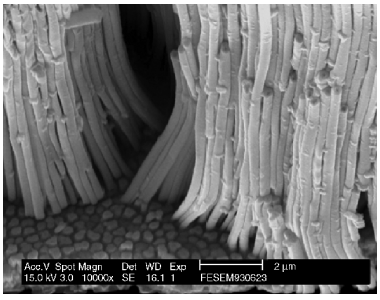

Side view image of $PbTiO_3$ nanowires bundle together after removing the AAO template.

Thermal decomposition of iron(VI) oxides, K_2FeO_4 and $BaFeO_4$, in an inert atmosphere

János Madarász, Radek Zbořil, Zoltán Homonnay, Virender K. Sharma and György Pokol

Page 1426

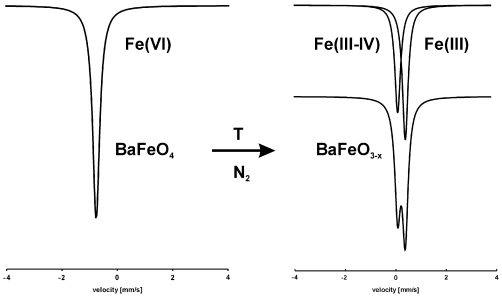

Thermal decomposition of iron(VI) oxides.

Synthesis and characterization of $Sr_{0.75}Y_{0.25}Co_{1-x}M_xO_{2.625+\delta}$ (M = Ga, $0.125 \leqslant x \leqslant 0.500$ and M = Fe, $0.125 \leqslant x \leqslant 0.875$)

F. Lindberg, O.A. Drozhzhin, S.Ya. Istomin, G. Svensson, F.B. Kaynak, P. Svedlindh, P. Warnicke, A. Wannberg, A. Mellergård and E.V. Antipov

Page 1434

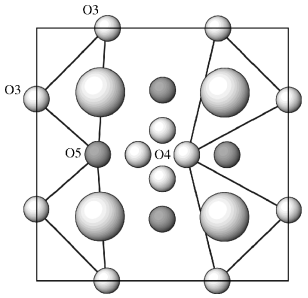

A possible arrangement of oxygen atoms in the oxygen-deficient layer of $Sr_{0.75}Y_{0.25}Co_{0.5}Fe_{0.5}O_{2.625+\delta}$ having crystal structure of perovskite related tetragonal phase $Sr_{0.75}Y_{0.25}CoO_{2.625}$ with unit cell parameters: $a = 2a_p$, and $c = 4a_p$ (314 phase).

Continued

Improvement of Er^{3+} emissions in oxyfluoride glass ceramic nano-composite by thermal treatment

Daqin Chen, Yuansheng Wang, Yunlong Yu and En Ma

Page 1445

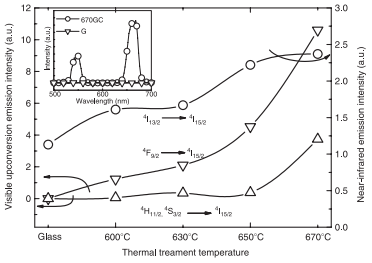

With increasing thermal treatment temperature, the emission intensities of $^4I_{13/2} \rightarrow {}^4I_{15/2}$, $^4F_{9/2} \rightarrow {}^4I_{15/2}$, and $^2H_{11/2}$, $^4S_{3/2} \rightarrow {}^4I_{15/2}$ transitions under 980 nm excitation are monotonously enhanced due to the incorporation of Er^{3+} into CaF_2 nano-crystals homogeneously precipitated among glass matrix.

Structure-inheriting solid-state reactions under hydrothermal conditions

Kazuo Eda, Yuichi Uno, Noriko Nagai, Noriyuki Sotani, Chen Chen and M. Stanley Whittingham

Page 1453

The present structure-inheriting solid-state reaction (SISSR) under a hydrothermal condition (ca. 10 bars and 453 K) enables us to markedly reduce the severe conditions for the usual synthesis of hp-$CoMoO_4$ via a solid-state phase transition (50 kbars and ca. 900 K).

Hydrothermal synthesis, crystal structure, thermal behavior, ferromagnetic resonance and ferrimagmetic behavior of $(C_4H_{12}N_2)_{1.5}[Fe_3(HAsO_4)_{1.02}(HPO_4)_{0.98}(AsO_4)_{0.88}(PO_4)_{0.12}F_5]$

Begoña Bazán, José L. Mesa, José L. Pizarro, Luis Lezama, A. Peña, María I. Arriortua and Teófilo Rojo

Page 1459

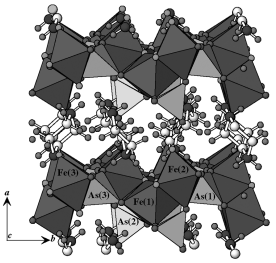

Layered crystal structure of $(C_4H_{12}N_2)_{1.5}[Fe_3(HAsO_4)_{1.02}(HPO_4)_{0.98}(AsO_4)_{0.88}(PO_4)_{0.12}F_5]$.

The defect chemistry of $Ce(Pr, Zr)O_{2-\delta}$

D.P. Fagg, J.R. Frade, V.V. Kharton and I.P. Marozau

Page 1469

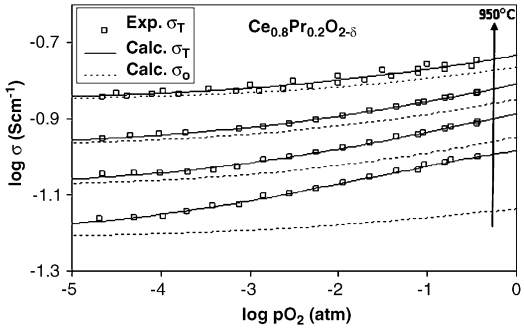

Oxygen partial pressure dependence of total conductivity of $Ce_{0.8}Pr_{0.2}O_2$ at 950, 900, 850, 800 °C, in oxidising conditions (arrows indicate direction of increasing temperature), dashed and solid lines indicate fit to experimental data (points).

Hydrothermal synthesis and characterization of the first 1-D indiumphosphate chain $In_2(HPO_4)_2(H_2PO_4)_2F_2 \cdot C_4N_2H_{12}$, a precursor for high dimensional structures

Chao Chen, Zhuo Yi, Minghui Bi, Yunling Liu, Chunyu Wang, Li Liu, Zan Zhao and Wenqin Pang

Page 1478

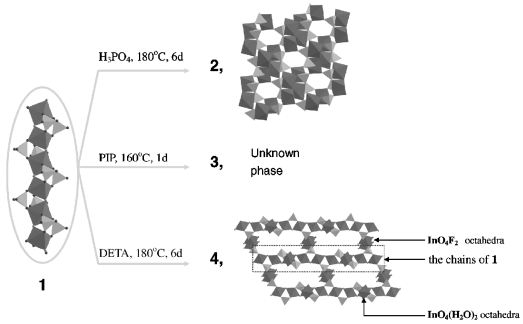

A first 1-D indiumphosphate chain has been prepared by hydrothermal technique and the dimensional transformation was investigated, which proved the chain could be as a precursor to form high-dimensional complex open-framework.

Zirconium scandium oxide nitrides: Formation and decomposition followed in situ by XRD and thermal analysis

N.J. Martinez Meta and E. Schweda

Page 1486

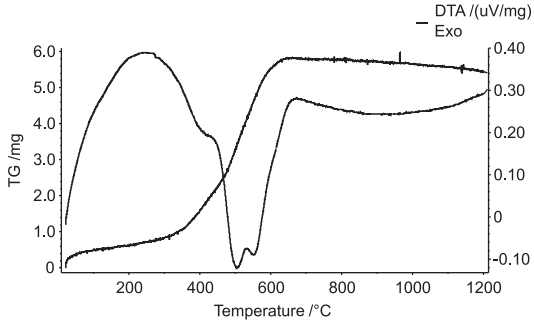

TG and DTA for the reoxidation of $Zr_{50}Sc_{12}O_{43}N_{50}$ to $Zr_{50}Sc_{12}O_{118}$ on air at a heating rate of 2 K.

A Raman spectroscopic study of the phase transition of $BaZr(PO_4)_2$: Evidence for a trigonal structure of the high-temperature polymorph

Thorsten Geisler, Karin Popa, Rudy J.M. Konings and Aurelian F. Popa

Page 1490

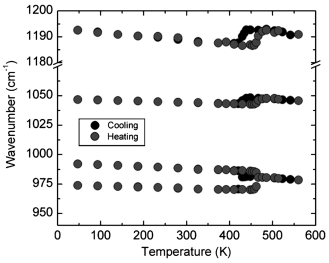

Raman mode frequencies of the PO_4 stretching vibrations in $BaZr(PO_4)_2$ as a function of temperature during heating and cooling across the phase transition temperature near 730 K.

A novel cobalt(II)–molybdenum(V) phosphate organic–inorganic hybrid polymer

Fa-Nian Shi, Filipe A. Almeida Paz, Penka I. Girginova, Helena I.S. Nogueira, João Rocha, Vítor S. Amaral, Jacek Klinowski and Tito Trindade

Page 1497

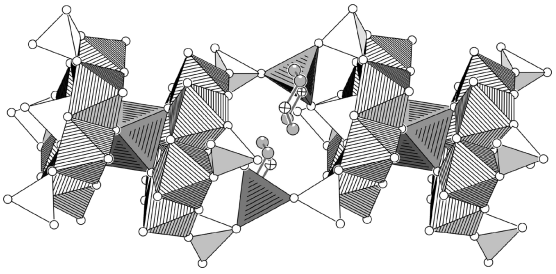

A new organic–inorganic hybrid cobalt(II)–molybdenum(V) phosphate hybrid polymer, $(H_2pip)_3[Co_3Mo_{12}O_{24}(OH)_6(PO_4)_8(H_{1.5}pip)_4]\cdot 5(H_2O)$ [where pip = piperazine], was isolated using hydrothermal synthesis, and characterised structurally by single-crystal X-ray diffraction, thermogravimetric analysis and vibrational spectroscopy. The magnetic properties of the material were also investigated.

Structure and physical properties of nonstoichiometric rare-earth cadmium antimonides, $RECd_{1-x}Sb_2$ (RE = La, Ce, Pr, Nd, Sm)

Andriy V. Tkachuk, Oksana Ya. Zelinska and Arthur Mar

Page 1506

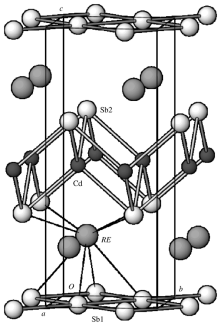

$RECd_{1-x}Sb_2$ adopts the $HfCuSi_2$-type structure, with layers of condensed $CdSb_4$ tetrahedra and Sb square nets.

A study of carboxylic-modified mesoporous silica in controlled delivery for drug famotidine

Qunli Tang, Yao Xu, Dong Wu and Yuhan Sun

Page 1513

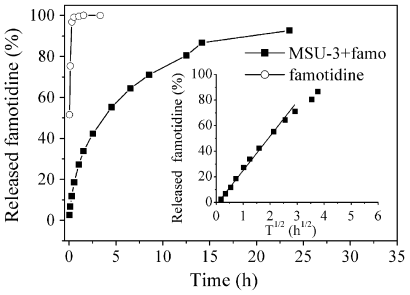

Famotidine dissolution curves and famotidine release profiles from the MS U-+famo in the solution of simulated body fluid. Inset: correlation of the percent of released famotidine vs. the square root of leaching time $t^{1/2}$.

Electrochemical immobilization of Cs in single-crystalline SYNROC

Hideki Abe, Akira Satoh, Kenji Nishida, Eiji Abe, Takashi Naka, Motoharu Imai and Hideaki Kitazawa

Page 1521

Optical microscope image of crystals grown at the tip of the working electrode.

The intercalation of cetyltrimethylammonium cations into muscovite by a two-step process: II. The intercalation of cetyltrimethylammonium cations into Li-muscovite

Xiaofeng Yu, Liyan Zhao, Xiuxiang Gao, Xiaoping Zhang and Nianzu Wu

Page 1525

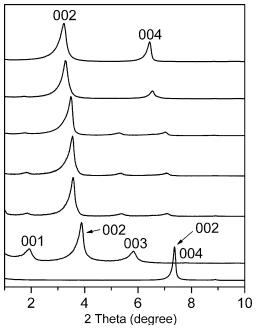

The CTA^+-intercalated muscovite composite with ordered structure has been obtained.

Continued

Two fluorescent coordination polymers constructed from mixed rigid and flexible carboxylate ligands: Formation of cross-linking helical and zigzag chains
Zhen Wang, Hanhui Zhang, Yiping Chen, Changcang Huang, Ruiqing Sun, Yanning Cao and Xiaohong Yu
Page 1536

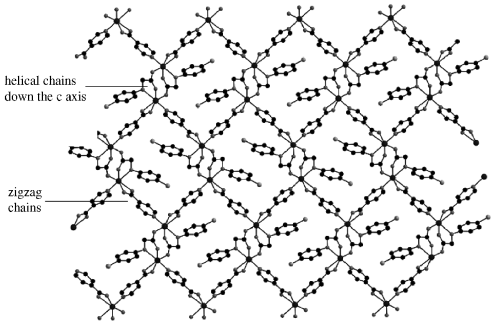

View of structure of complex **2** down the *c*-axis, showing the cross-linking of helical chain units and zigzag chain uints. Hydrogen atoms were removed for clarity.

Syntheses and crystal structures of three new borates templated by transition-metal complexes in situ
Guo-Ming Wang, Yan-Qiong Sun and Guo-Yu Yang
Page 1545

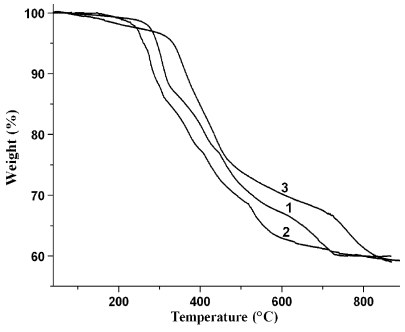

TG curve of **1–3**.

Synthesis of maghemite sub-microspheres by simple solvothermal reduction method
Xian-Ming Liu, Shao-Yun Fu and Hong-Mei Xiao
Page 1554

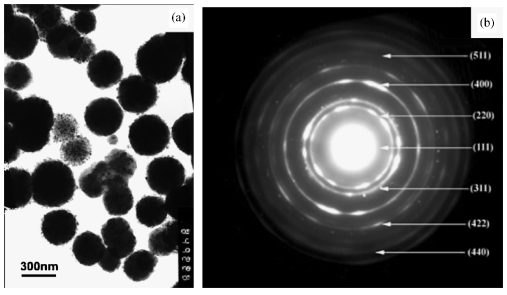

TEM photograph (a) and ED pattern (b) of the sample.

Hydrothermal synthesis and crystal structure of a new inorganic/organic hybrid of scandium sulfate: $(H_2en)Sc_2(SO_4)_4 \cdot (H_2O)_{0.72}$
Jianjiang Lu, John A. Schlueter and Urs Geiser
Page 1559

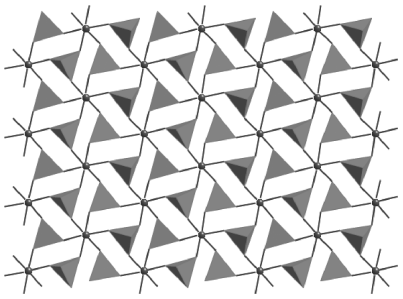

The first organically templated layered structure of scandium sulfate, $(H_2en)Sc_2(SO_4)_4 \cdot (H_2O)_{0.72}$, (en = ethylenediamine) was synthesized by a hydrothermal method and characterized by single crystal X-ray diffraction. Thermogravimetric analysis indicates that this material is thermally stable to above 400 °C.

Preparation and electrorheological properties of triethanolamine-modified TiO_2
J.G. Cao, M. Shen and L.W. Zhou
Page 1565

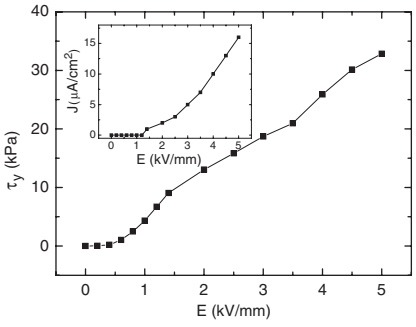

The yield stress and current of triethanolamine-modified TiO_2 under DC electric field.

The intercalation of cetyltrimethylammonium cations into muscovite by a two-step process: I. The ion exchange of the interlayer cations in muscovite with Li^+
Xiaofeng Yu, Liyan Zhao, Xiuxiang Gao, Xiaoping Zhang and Nianzu Wu
Page 1569

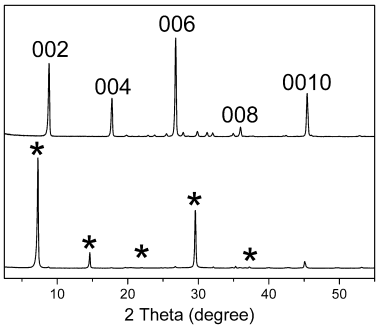

Powder XRD diffraction patterns of original muscovite and muscovite after the first $LiNO_3$ treatment.

Bi_2Te_3–Te nanocomposite formed by epitaxial growth of Bi_2Te_3 sheets on Te rod
Yuan Deng, Chang-Wei Cui, Ni-La Zhang, Tian-Hao Ji, Qing-Lin Yang and Lin Guo
Page 1575

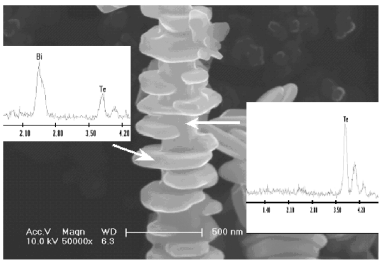

SEM image of an individual sheet-rod with EDX patterns (inset) taken from sheet and rod indicated by arrows.

Computational study of cation substitutions in apatites
Toomas Tamm and Merike Peld
Page 1581

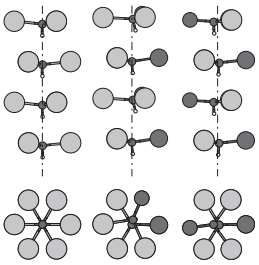

Deformation of the hydroxide ion chain due to substitutions around the ion channel in substituted hydroxyapatites.

Crystal chemistry and crystallography of the SrR_2CuO_5 (R = lanthanides) phases
W. Wong-Ng, T. Haugan, J.A. Kaduk, R.A. Young, Z. Yang, M.H. Jang and M. Luong
Page 1588

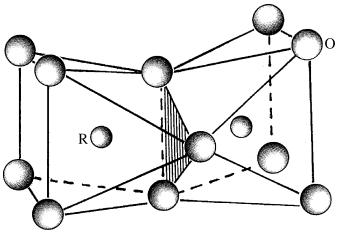

Seven-fold coordination of R in SrR_2CuO_5 (R = lanthanides) is shown inside a monocapped trigonal prism. Two such RO_7 units are joined to form the basic structure motif of R_2O_{11}.

Syntheses, structures, and magnetic properties of the europium(II) selenido pnictogenates(III), $EuPnSe_3$ (Pn = Sb, Bi)
Geng Bang Jin, Shane J. Crerar, Arthur Mar and Thomas E. Albrecht-Schmitt
Page 1596

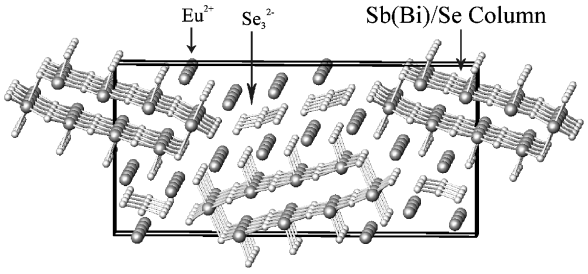

The isotypic compounds, $EuPnSe_3$ (Pn = Sb, Bi), have been prepared as pure phases via the reaction of Eu with Pn_2Se_3 (Pn = Sb, Bi) and Se. Their structures consist of square pyramidal $PnSe_5$ units and distorted $PnSe_6$ octahedra that form hollow columns that are separated by Eu^{2+} cations and Se_3^{2-} anions.

Effects of Al-doping on the stabilization of monoclinic $LiMnO_2$
Zu-Fei Huang, Chun-Zhong Wang, Xing Meng, Deng-Pan Wang and Gang Chen
Page 1602

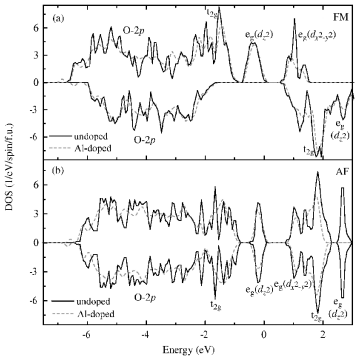

Total density of states (DOS) around E_F (0 eV) without and with Al-doping for the (a) FM and (b) AF solutions. Spin-up/down states are plotted along the positive/negative ordinate.

NOTICE

The Keyword Index for Volume 179 will appear in the December 2006 issue as part of a cumulative index for the year 2006.